Revision 1

Uranium scavenging during mineral replacement reactions

Kan Li,[1] Allan Pring,[2,4] Barbara Etschmann,[1,2,7] Edeltraud Macmillan,[3] Yung Ngothai,[1] Brian O'Neill,[1] Anthony Hooker,[1,5] Fred Mosselmans,[6] and Joël Brugger[2,7*]

[1]School of Chemical Engineering and [3]School of Earth and Environmental Sciences, The University of Adelaide, 5000, South Australia, Australia
[2]Division of Mineralogy, South Australian Museum, North Terrace, 5000, Adelaide, South Australia, Australia
[4]School of Chemical and Physical Sciences, Flinders University, 5001, South Australia, Australia
[5]Radiation Health, Radiation Protection Branch, Environment Protection Authority, Victoria SQ, 5000, Adelaide, South Australia, Australia
[6]Diamond Light Source Ltd, Diamond House, Harwell Science and Innovation Campus, Didcot, Oxfordshire, UK, OX11, 0DE
[7]School of Earth, Atmosphere and Environment, Monash University, 3800, Clayton, Victoria, Australia

*Corresponding author: joel.brugger@monash.edu

Abstract

Interface coupled dissolution-reprecipitation reactions (ICDR) are a common feature of fluid-rock interaction during crustal fluid flow. We tested the hypothesis that ICDR reactions can play a key role in scavenging minor elements by exploring the fate of U during the experimental sulfidation of hematite to chalcopyrite under hydrothermal conditions (220-300 ˚C). The experiments where U was added, either as solid UO_{2+x}(s) or as a soluble uranyl complex, differed from the U-free experiments in that pyrite precipitated initially, before the onset of chalcopyrite precipitation. In addition, in UO_{2+x}(s)-bearing experiments, enhanced hematite dissolution led to increased porosity and precipitation of pyrite+magnetite within the hematite core, whereas in uranyl nitrate bearing experiments, abundant pyrite formed initially, before being replaced by chalcopyrite. Uranium scavenging was mainly associated with the early reaction stage (pyrite precipitation), resulting in a thin U-rich line marking the original hematite grain surface. This 'line' consists of nanocrystals of UO_{2+x}(s), based on chemical mapping and XANES spectroscopy. This study shows that the presence of minor components can affect the pathway of ICDR reactions. Reactions between U- and Cu-bearing fluids and hematite can explain the Cu-U association prominent in some iron oxide-copper-gold (IOCG) deposits.

Keywords: uranium, scavenging, IOCG deposits, experiment, sulfidation reaction, interface coupled dissolution-reprecipitation reactions.

Introduction

Iron oxide-copper-gold (IOCG) deposits, such as Olympic Dam (OD) and Prominent Hill in South Australia, are important sources of copper, uranium, gold, and silver. Uranium is always enriched in South Australian IOCG ores, acting as a penalty element or a resource depending on grade and distribution. OD is characterized by a relatively oxidized mineral assemblage; magnetite-pyrite precipitated at the periphery of the deposit, and hematite dominates in the ores, with a barren hematite body forming the core of the deposit. Copper minerals show an increase in Cu:S ratio towards the core of the deposit: chalcopyrite dominates at the periphery, followed by bornite and finally chalcocite. Bastrakov et al. (2007) suggested that the mineralogical zoning at OD and the stable isotopic (O, S) composition of ore minerals is consistent with a two stage model, whereby a hot, highly saline fluid (>30 wt% NaCl; > 400 ˚C) sourced from a granitic magma formed a low-grade, relatively reduced, magnetite-chalcopyrite orebody, which was later remobilized and upgraded by interaction with meteoric, oxidized fluids.

Although OD is the World's largest U deposit in terms of metal endowment, no specific study on the genesis of U mineralization has been conducted (Cuney, 2009). Leaching of U from the wall rocks and reaction of the U-bearing hydrothermal fluids with the Fe-oxide and Cu-sulfide mineralization is assumed to be responsible for U enrichment in some IOCG deposits by a factor of 10 to 40 relative to the fresh host rocks (Hitzman et al., 1992; Hitzman and Valenta, 2005). In contrast to the Cu-bearing minerals, the U-bearing minerals do not show a clear zonation pattern at OD. Uranium minerals occur throughout the Cu-enriched zone; uraninite is associated mainly with Cu-Fe sulfides and hematite; brannerite and coffinite are associated mainly with sulfides, quartz, and sericite (Cuney, 2009).

The importance of fluid-mediated interface coupled dissolution reprecipitation (ICDR) reactions in geological processes has been emphasized over the past decade (Putnis, 2009; Putnis and John, 2010). These reactions are key to understanding ore formation processes, grade control, and the evolution of ore textures, e.g., alteration of pentlandite in the cementation zone (Tenailleau et al., 2006); replacement of magnetite and pyrrhotite by Fe-sulfides (Qian et al., 2010); hematite by chalcopyrite and bornite (Zhao et al., 2014); scavenging of bismuth and gold during ICDR reactions (Tooth et al., 2011); or reactions involving Au-Ag-tellurides (Okrugin et al., 2014; Zhao et al., 2009; 2013); or Fe-Ti oxides (Janssen et al. 2010, 2011). Replacement reactions are prominent in IOCG deposits, involved in local and regional alteration, and in upgrading of the Cu and U ores via reaction with preexisting iron-oxide ores.

The aim of this study is to test the hypothesis that U is scavenged from the hydrothermal fluids during ICDR reactions, helping to elucidate the Cu-U association in IOCG deposits. We used the replacement of hematite by chalcopyrite under hydrothermal conditions as a model reaction, as this reaction was recently studied by Zhao et al. (2014). Understanding the processes that scavenge U during fluid-rock interaction is key not only for understanding the distribution of U in these deposits, but also for addressing the potential effect of ICDR reactions in promoting or inhibiting metal recovery during ore processing via hydrometallurgical or *in-situ* leaching methods.

Starting materials

Hematite sulfidation experiments in the presence of sulfur were conducted following the method of Zhao et al. (2014), by reacting hematite, copper(I) chloride,

and thioacetamide in the presence of water at 220 and 300 °C, P_{sat}. Analytical grade CuCl (Hopkin and Williams Ltd.) purified using the procedure of Keller et al. (1946), and thioacetamide (CH_3CSNH_2) (Scharlau Chemie SA) were used in the experiments. Thioacetamide is stable at room temperature, but it decomposes above 100 °C and releases H_2S. The solution pH at the reaction temperature was buffered by the HS^-/H_2S(aq) buffer. To better constrain the pH, we added sodium acetate (0.14 m) and acetic acid (0.059 m) to shift the HS^-/H_2S(aq) buffer, as well as 1 molal NaCl to prevent disproportionation of Cu(I) complexes (Zhao et al., 2014). Using the HCh thermodynamic equilibrium program (Shavarov, 1999), a $pH_{300°C}$ of 5.89 was calculated for the system that consisted of 0.0025 moles H_2S and HN_3, 0.000295 mole CH_3COOH, 0.0007 mole CH_3COO Na, 10 mg hematite and 12.5 mg CuCl in 5 ml H_2O. Uranium was introduced as uraninite (see below) or uranyl nitrate (H.B. Selby and Co. Pty. Ltd).

Hematite (SA Museum collection number G6983) was used as the starting material. The identification and composition of this mineral was checked by powder X-ray diffraction (XRD; Huber Guinier Imaging Plate G670 with Co $K\alpha_1$ radiation) and by electron probe microanalysis (Cameca SX-52 operated at 20 kV, 20 nA). The following probe standards were used: Fe_2O_3 and Fe_3O_4 (Fe); $Mg_3Al_2(SiO_4)_3$ (Si, Al and Mg); $Ca_5(PO_4)_3F$ (P); $MnSiO_3$ (Mn) and V metal (V). The analysis of hematite (10 points) showed that the starting material was pure (>99.5% hematite components), although some crystals contained micro-inclusions of silica (apparent SiO_2 contents up to 3.0 wt%). Crystals were washed ultrasonically, ground and sieved into 125 to 150 µm size fractions.

Synthetic uraninite was used for the experiments. It was produced by the reduction of high purity $UO_2(NO_3)_2$ by Zn metal as follows: $UO_2(NO_3)_2$ was dissolved in 1 molar HCl; O_2(aq) was removed by bubbling a 99.5% N_2 and 0.5% H_2 gas mixture through the solution, which was then sealed into Teflon-lined autoclaves. The autoclaves were kept at 150 °C for 3 days. After cooling, the products were washed in 10 molar HCl several times until no further bubbles were released in order to remove Zn and U(VI) impurities. Finally, the products were washed in Milli-Q water (conductivity of 18 MΩ cm^{-1}, Direct-Q3 system, Millipore Corp) and acetone. The synthetic uraninite has a unit cell size a = 5.4105(2) Å (V = 158.38(2) $Å^3$), as refined using TOPAS (Bruker, 2005). This unit cell dimension is typical for uraninite found in hydrothermal environments (Fritsche and Dahlkamp, 1997), and corresponds to a uraninite composition $UO_{2.56}$ (Grønvold, 1955; Singh et al., 2011).

Experiments and characterization

Hematite (10 mg), CuCl(s) (12.3 mg), CH_3CSNH_2 (187.5 mg), and either uraninite (80 mg) or $UO_2(NO_3)_2$(s) (116.7 mg, corresponding to ~3,000 ppm U in solution), were loaded into Ti-autoclaves with an 8 ml internal volume in an argon-filled glove box together with 5 ml of a 0.2 m acetate buffered solution. All hydrothermal runs were performed in electric muffle furnaces at 220 and 300 °C (temperature controlled within ±1 °C). After reaction, the autoclaves were quenched in a large volume (~10 L) of cold water for 45 minutes. The reacted fluid was collected, and solids were rinsed three times with Milli-Q water and then once with acetone before drying.

A Philips XL30 field emission scanning electron microscope (FESEM) was

used to characterize the surface morphology of the grains (secondary electron mode, SE). Chemical features were checked using backscattered electrons (BSE) and energy dispersive X-ray spectrometry (EDAX). A FEI Helios NanoLab DualBeam Focussed Ion Beam FIB-SEM (FEI, Netherlands) was used to prepare cuts and extract thin sections (10 x 10 x 5 μm^3) from well-controlled areas within the samples (Fig. 1). Ablation was performed using a Ga beam (20-30 kV/0.093-0.21 nA). Chemical maps were also obtained using the instrument's EDAX system.

Uranium L_{III}-edge X-ray absorption near edge structure (XANES) spectra were collected at beamline I18 at the Diamond Light Source, Oxfordshire, UK. I18 is an undulator beam line with a Si(111) double crystal monochromator; at 17 keV the energy resolution was ~2.4 eV (1.4 x 10^{-4}) and the flux ~10^{10} photons/s. The beam was focused to a size of ~6 x 2.2 μm^2 using KB mirrors, and fluorescence data was collected with a 9 element Ge detector. The energy was calibrated using a Y foil (first derivative maximum at 17,038 eV for the Y K-edge).

Results

U-free runs

Experiments were conducted at 220 and 300 ˚C for reaction times between 2 hours and 2 weeks, and chalcopyrite rims formed around hematite grains in all runs. Only trace amounts of chalcopyrite were observed for reaction times shorter than 1 week, and the amount of chalcopyrite increased with increasing reaction time; however after two weeks no further change in the reaction products was observed, consistent with the results of Zhao et al. (2014). A 10-20 µm thick rim of chalcopyrite was produced around the hematite grains after 2 weeks at 300 ˚C

(Fig. 1a). The hematite cores showed no sign of reaction or dissolution. The chalcopyrite rim grew both via the replacement of chalcopyrite and via overgrowth on the outside of the rim (Zhao et al., 2014). The boundary between these two types of chalcopyrite is marked by a line of high porosity, which was labeled in Fig. 1a.

$UO_{2+x}(s)$ as uranium source

The textures obtained in experiments where synthetic uraninite was added as a U source are generally similar to those obtained in the U-free experiments, with a chalcopyrite rim surrounding the hematite grains (Fig. 1b). However, SEM images reveal a mottled texture in the hematite cores, which is due to the partial replacement of hematite by pyrite and magnetite, as confirmed by XRD results; this contrasts with the U-free runs, in which the hematite core showed no evidence of mineralogical change.

SEM imaging shows that U is present in the reacted grains in two different forms: (i) uraninite grains enclosed in the chalcopyrite overgrowth (Fig. 1b), and (ii) a thin line (≤ 1 µm) between the chalcopyrite rim and the original grain (Figs. 1b,c) that consists of U-rich nano-crystals. Thus, after two weeks reaction time, from the outside of the grains, there is a ~10 µm thick chalcopyrite rim containing patches of uraninite; a thin U-rich layer, and a hematite core with small patches of magnetite and pyrite. In order to observe the reaction interfaces deep within the grain, a FIB slice was cut across part of the grain crossing three phases; the location of this cut is indicated by a red line on Fig. 1b. Porosity is evident within the hematite core (left side in Fig. 1c), a result of the patchy replacement of hematite by pyrite and magnetite in the grain. An EDAX chemical map shows that the U-rich line marks the boundary between a thin pyrite rim and the chalcopyrite rim (Fig. 1d). Also note the

absence of porosity at the pyrite-chalcopyrite boundary, which suggests that U is not a quenching feature, as U would be expected to be associated with remaining porosity if it was depositing from trapped solution during quenching.

We performed additional experiments to confirm that the presence of uraninite caused the enhanced reactivity of the hematite core (Fig. 2). No reaction was observed when hematite was heated in a buffer solution at 300 ˚C for 1 week. Addition of uraninite (hematite+buffer+UO_{2+x}(s) system) resulted in enhanced dissolution of hematite (Fig. 2a,b). Finally, addition of thioacetamide (hematite+buffer+UO_{2+x}(s)+thioacetamide system) resulted in textures (Figs. 2c,d) that were similar to those in the hematite+buffer+UO_{2+x}(s)+thioacetamide+CuCl system (Figs. 1b,c), with the difference that the mottled cores of the hematite are surrounded by pyrite rims rather than chalcopyrite. Similarly to chalcopyrite, pyrite appears to both directly replace hematite (Fig. 2d) and to form via overgrowth, encapsulating some of the added uraninite particles (Fig. 2c); aside from these encapsulated uraninite particles, the pyrite overgrowths are U-free (Fig. 2d). A sub-μm thick U-rich layer marks the contact between the two types of pyrite (Figs. 2c,d). The pyrite replacing hematite displays the same porosity as the parent hematite, but some of this porosity appears to be partially filled with a U phase (Fig. 2d). This suggests that the pyrite replacement occurred after hematite dissolution had taken place.

$UO_2(NO_3)_2$ as uranium source

Experiments using soluble $UO_2(NO_3)_2$ as the U source (Fig. 3) differed from those using uraninite in three ways. (i) The hematite core showed no evidence of reaction, i.e. no pyrite or magnetite and no increase in porosity was observed (e.g.,

Fig. 3c). (ii) Compared to the uraninite experiments, the uranium-rich layers after two weeks reaction time at 300 ˚C were usually thicker (<3 µm in width versus < 1µm) and precipitated at the surface of the original hematite grains, now marking the contact between replacing and overgrowth chalcopyrite. Some of the uranium-rich layers were also present within the overgrowing chalcopyrite (Fig. 3c,d,e). (iii) Pyrite appears as patches within the chalcopyrite rims on the inside of the uranium-rich layers (i.e., within chalcopyrite formed via direct replacement of hematite); after two weeks reaction time, no pyrite was detected on the outer side of the uranium-rich layer, i.e. within the chalcopyrite overgrowth (Fig. 3c,d,e), indicating the replacement of pyrite by chalcopyrite over time. After a short reaction time of 2 hours at 300 ˚C (Fig. 3a,b), the only sulfide mineral observed was a thin (< 5 µm) rim of pyrite (based on EDAX analyses), which contains a uranium-rich layer as well as U-rich nanoparticles (detail in Fig. 3b).

XANES spectroscopy

It is essential to identify the oxidation state of the uranium in the reacted grain to be able to determine the reaction mechanism. XANES can be used to determine the speciation and oxidation state of trace elements in minerals *in-situ* with µm-scale spatial resolution (Brugger et al., 2008; 2010). The average oxidation state of U can be retrieved from the U L_{III}-edge XANES spectra by measuring the position of the white line that shifts by 3.75–4.3 eV from U^{4+} to U^{6+} (Bertsch et al., 1994; Yamamoto et al., 2008), or the presence of a band at around 17,232 eV related to uranyl resonance (Conradson, 1998). For this study it was sufficient to compare the XANES spectra of experimental samples with those of two U mineral standards: saleeite, ($Mg(U^{6+}O_2)(PO_4)_2 \cdot 10H_2O$, Ranger Mine, Northern Territory, Australia, Museum Victoria Sample M41723; and cleusonite, Pb (U^{4+}, U^{6+})

240 $(Ti,Fe^{2+},Fe^{3+})_{20}\bullet(H_2O)_{38}$, Cleuson, Valais, Switzerland, Wülser et al. (2005), South
241 Australian Museum sample G29393. Saleeite contains U^{6+} as a uranyl ion UO_2^{2+};
242 and cleusonite is nominally a U^{4+} mineral, although it may contain small amounts of
243 U^{6+}/U^{5+} due to radiation damage and weathering. XANES spectra were measured on
244 a FIB slice cut from the sample (Fig. 1b), which made it possible to analyze the
245 uranium-rich layer without contamination from the uraninite inclusions. Comparison
246 of the three spectra confirmed that the dominant uranium oxidation state in the U-
247 rich layers is U^{4+} rather than U^{6+} (Fig. 4). The shift of the white line to lower energy
248 by ~4 eV between saleeite and the synthetic samples confirms that the latter consist
249 predominantly of U^{4+} (Bertsch et al., 1994; Yamamoto et al., 2008).

250 ## Discussion

251 Addition of uranium during the sulfidation of hematite from Cu-rich
252 solutions under hydrothermal conditions results not only in the scavenging of U at
253 specific stages of the replacement reaction, but also in changes in the reaction
254 pathways depending on the U source. In this discussion we aim to elucidate the
255 mechanisms that drive the differences and their role in uranium scavenging.

256 ### *Effect of uranium on the reaction within the hematite core*

257 The hematite cores appear to remain unreacted in experiments conducted
258 with no U or when uranyl nitrate was used as a U source; however, when uraninite
259 was used as a U-source, the hematite cores displayed enhanced porosity and patchy
260 areas of replacement by pyrite and magnetite (Figs. 1a,b,c; 3a). This indicates that in
261 the presence of uraninite, insoluble Fe^{3+} can be reduced to soluble Fe^{2+}, for example
262 via the two half reactions:

(1a) UO_2 (uraninite) $\rightarrow UO_2^{2+}(aq) + 2e^-$

(1b) Fe_2O_3 (hem) + 6 $H^+ + 2e^- \rightarrow 2Fe^{2+} + 3H_2O$

U^{4+} can readily be oxidized to U^{6+} by Fe^{3+} (Nevin and Lovley, 2000). Once Fe^{2+} is released into solution, some of it will move into the bulk solution, accounting for increased porosity in the hematite. Some will react with hematite to form magnetite:

(2) $Fe^{2+}(aq) + Fe_2O_3$ (hem) + $H_2O \rightarrow Fe_3O_4$ (mag) + $2H^+$

In S-bearing experiments, some of the Fe^{2+} reacted with the dissolved sulfur to form pyrite. This is an oxidation reaction, as S in solution is present as hydrosulfide (e.g., $[H_2S^{-II}](aq)$), while pyrite contains $[S^{-I}_2]^{2-}$ dimers.

(3) $Fe^{2+}(aq) + 2HS^-(aq) \rightarrow FeS_2(py) + 2H^+ + 2e^-$

Possible oxidants required to balance reaction **(3)** include uranyl complexes (e.g., via equation **(1a)** and reduction to uraninite) and Fe^{3+}-bearing minerals (e.g., equation **(1b)**), as well as polysulfides formed by oxidation of the hydrosulfide species (Qian et al. 2010; Rickard and Luther, 2007). As U(IV) minerals are poorly soluble, reduction of uranyl complexes is unlikely to explain pyrite precipitation within the hematite core.

Effect of uranium on the replacement reaction and uranium scavenging

Chalcopyrite rims along the parent grains were observed from all three series of experiments; the only exception was the run for 2 hours using uranyl nitrate, in which pyrite was the only sulfide observed rimming hematite. Whereas chalcopyrite was the only mineral detected in the reaction rims in the U-free runs, pyrite was

present in the runs containing either uranyl in solution or UO_{2+x}(s). In the U-free reactions (Fig. 1a), the overall process of forming chalcopyrite can be represented as:

(4) Fe_2O_3 (hem) + $2Cu(HS)_2^-$(aq) + $2H^+ \rightarrow 2FeCuS_2$ (cpy) + $3H_2O$

Note that the overall reaction **(4)** is not a redox reaction, and that it is associated with a large volume increase (Zhao et al. 2014). As a result, chalcopyrite grows both as pseudomorphic replacement of hematite via an ICDR mechanism and via overgrowth on the outside of the grains (Zhao et al., 2014).

The replacement of hematite by pyrite in the U-bearing experiments is overall an oxidation reaction:

(5) Fe_2O_3 (hem) + $4HS^-$(aq) + $2H^+ \rightarrow 2FeS_2$ (py) + $3H_2O$ + $2e^-$

Most likely, this reaction is linked to the reduction of some hematite (equation **1b**) or of some uranyl in solution (which is present even when UO_{2+x}(s) is the U source). The lack of significant U scavenging during pyrite formation suggests that the main oxidant is hematite, but the association between pyrite and the presence of uranium in the system indicates that uranyl may act as a catalyst to promote the nucleation of pyrite versus that of chalcopyrite. We also tested the hypothesis that the higher proportion of pyrite found in experiments conducted using uranyl nitrate were due to the reduction of nitrate at temperature (Brandes et al 2008), but found no pyrite under U-free-reaction with sodium nitrate at 300 ˚C after 2 and 24 hours. In experiments where soluble uranyl nitrate is the source of uranium, after 2 hours of reaction time there was no chalcopyrite but only a thin pyrite rim enriched in uranium (Fig. 3a,b). After more that one week reaction time, these runs show patchy areas of pyrite within a chalcopyrite rim; these patches are located on the inside of

the uranium-rich layer, i.e. they occur within the chalcopyrite that replaces hematite rather than in the chalcopyrite overgrowth (Fig. 3c,d,e). This confirms the role of uranyl in the formation of pyrite, as higher concentrations of uranyl in the experiments conducted using $UO_2(NO_3)_2$ resulted in more extensive pyrite precipitation than in those where UO_{2+x}(s) was the U source.

Pyrite was replaced by chalcopyrite in the latter stages of the $UO_2(NO_3)_2$ runs. This reaction is common in massive-sulfide deposits (e.g., Badrzadeh et al. 2011; Slack et al. 2003). The replacement of pyrite by chalcopyrite involves the oxidation of Fe^{2+} (pyrite) to Fe^{3+} (chalcopyrite; e.g. Cook et al. 2012), and reduction of the disulfide ion (pyrite) into sulfide (chalcopyrite). The fast reaction rate is consistent with the ICDR reaction mechanism. The dissolution of pyrite can be presented as reaction **(6)**, which releases a polysufide species into solution. The precipitation of chalcopyrite, assuming that S is sourced from the excess bisulfide in solution, is an oxidation reaction (reaction **7**). It can be balanced if part of the sulfur is sourced from the reduction of the polysulfide released by pyrite dissolution **(**reaction **8)**. The replacement of pyrite by chalcopyrite in our experiments and in many natural examples appears to preserve volume. Since the molar volume of chalcopyrite is about twice that of pyrite (47.7 and 23.95 $cm^3 \cdot mol^{-1}$, respectively), ~ ½ mole of pyrite results in the formation of 1 mole of chalcopyrite; the remaining half Fe^{2+} and S^- have to escape into solution. Reaction **(9)** illustrates the main overall reaction for isovolumetric pyrite replacement by chalcopyrite.

(6) FeS_2 (py) → $Fe^{2+} + S_2^{2-}$ (py dissolution)

(7) $Fe^{2+} + Cu(HS)_2^- \rightarrow CuFeS_2$ (cpy) + $2H^+ + e^-$ (oxidative cpy precipitation)

(8) ½ $S_2^{2-} + H^+ + e^- \rightarrow HS^-$ (reduction of disulfide ion)

(9)=(2*6+7+8) $2FeS_2$ (py) + $Cu(HS)_2^-$ → $CuFeS_2$ (cpy) + Fe^{2+} + $1.5S_2^{2-}$ + HS^- + H^+

A key feature of the U-bearing experiments is the presence of U-rich layers, formed by an accumulation of UO_{2+x}(s) nanocrystals, within the chalcopyrite (±pyrite) rims (Figs. 2d; 3b,d). This U enrichment appears to form early in the replacement reaction, and is often located at the interface between a thin pyrite layer and the chalcopyrite (Figs. 1c,d). Nucleation of pyrite follows significant dissolution of hematite, yet occurs at the early stage of the reaction, before chalcopyrite growth takes over. A coupling between the half reactions **(3)** and **(1a)**, whereby dissolved uranyl provides the oxidant for the formation of pyrite, provides an adequate mechanism to explain the coupling between pyrite formation and uraninite precipitation. It also explains that U-scavenging was more efficient in the experiments in which uranyl nitrate was added: the U-rich layer is ~0.3 μm thick in experiments conducted with UO_{2+x}(s), but 1.5 μm in those conducted using uranyl nitrate.

Implications for element scavenging and IOCG deposits

The replacement of hematite by chalcopyrite described by Zhao et al. (2014) resulted in a relatively simple mineralogy and homogeneous textures. Addition of uranium in the experiments caused additional complexity, by (i) increased hematite solubility in the presence UO_{2+x}(s); this also resulted in the formation of magnetite; and (ii) enabling pyrite to form as an early reaction product as a result of the presence of uranyl complexes in solution. Uranium scavenging was closely linked to the early pyrite precipitation, i.e. the reduction of uranyl in solution to form insoluble UO_{2+x}(s) was coupled to the oxidation of S^{2-} into S_2^{2-}. The uraninite was present in nanoparticulate form.

Hence, our experiments show that the interaction of uranyl-bearing fluids and Fe-oxide/sulfide assemblages is conducive to the precipitation of fine-grained uraninite. This is consistent with the association of fined grained and nanoparticulate uraninite with Cu-Fe sulfides and associated hematite at Olympic Dam (Ciobanu et al. 2013). The UO_{2+x}(s) layers formed in the experimental replacement reactions are similar to some of the uraninite textures found in the Olympic Dam deposit (Fig. 5). At Olympic Dam uraninite occurs in a wide variety of different textures and associations, suggesting that a number of processes were at play during uranium concentration, and consistent with extensive U-scavenging during fluid-mineral interaction. Tooth et al. (2011) present another example of scavenging of trace elements (Au,Bi) linked to fluid-rock interaction and ICDR reactions, showing that the oxidation of pyrrhotite into magnetite was linked to the reduction of aqueous Bi^{3+} into metallic Bi. At temperatures above the melting point of elemental Bi, aqueous Au^{+} complexes were scavenged by the Bi-melts (Cockerton and Tomkins, 2012; Tooth et al. 2008). Hence, Tooth et al. (2011) present the coupling as resulting from locally reducing conditions caused by the dissolution of pyrrhotite. In the present study, uranium was scavenged during hematite sulfidation, and the reduction of aqueous uranyl complexes was coupled with the replacement of hematite by pyrite, an oxidation reaction. A unique feature of the uranium scavenging reaction is its discontinuous nature; an initial burst in U-scavenging is followed by the growth of chalcopyrite with little U-scavenging. Overall, this study further emphasizes the significance of local (e.g., reaction front) conditions for controlling the metal budget in some ore deposits.

This study also illustrates how the presence of minor components can affect the pathway of ICDR reactions, and the nature and textures of the products formed.

Instead of being a by-product of the main replacement reaction, the reduction of uranyl appears to affect the nature of the reaction, causing precipitation of pyrite rather than chalcopyrite in U-free runs. Hence, the presence of minor components in solution (uranyl complexes in this case) can affect the nature of the reaction at the interface, in particular by acting as catalysts for promoting redox reactions. Given the dynamic nature of ore formation (Ord et al. 2012), such complex, non-equilibrium processes are expected to be widespread in ore deposits and affect the mineralogy and metal endowment of the ores.

Acknowledgements

We acknowledge Diamond Light Source, UK for access to the I18 beam line to undertake part of the research, as well as the Australian International Synchrotron Access Program for travel funding. This study was funded by the Institute for Mineral and Energy Resources (IMER), the Australian Research Council (grant DP1095069), and BHP Billiton. We also appreciate the help from Dr Animesh Basak (Adelaide Microscopy, Australia) with preparing FIB-cuts for synchrotron measurements.

References

Badrzadeh, Z., Barrett, T.J., Peter, J.M., Gimeno, D., Sabzehei, M., and Aghazadeh, M. (2011) Geology, mineralogy, and sulfur isotope geochemistry of the Sargaz Cu-Zn volcanogenic massive sulfide deposit, Sanandaj-Sirjan Zone, Iran. Mineralium Deposita, 46, 905-923.

Bastrakov, E.N., Skirrow, R.G., and Davidson, G.J. (2007) Fluid evolution and origins of iron oxide Cu-Au prospects in the Olympic Dam district, Gawler Craton, South Australia. Economic Geology, 102, 1415-1440.

Bertsch, P.M., Hunter, D.B., Sutton, S.R., Bajt, S., and Rivers, M.L. (1994) In situ chemical speciation of uranium in soils and sediments by micro X-ray absorption spectroscopy. Environmental science & technology, 28, 980-984.

Brandes, J.A., Hazen, R.M., and Yoder, H.S., Jr. (2008) Inorganic Nitrogen Reduction and Stability under Simulated Hydrothermal Conditions. Astrobiology, 8, 1113-1126.

Brugger, J., Etschmann, B., Pownceby, M., Liu, W., Grundler, P., and Brewe, D. (2008) Tracking the chemistry of ancient fluids: oxidation state of europium in hydrothermal scheelite. Chemical Geology, 257, 26-33.

Brugger, J., Pring, A., Reith, F., Ryan, C., Etschmann, B., Liu, W., O'Neill, B., and Ngothai, Y. (2010) Probing ore deposits formation: New insights and challenges from synchrotron and neutron studies. Radiation Physics and Chemistry, 79, 151-161.

Bruker, A. (2005) TOPAS V3: General profile and structure analysis software for powder diffraction data. User's Manual, Bruker AXS, Karlsruhe, Germany.

Ciobanu, C.L., Wade, B.P., Cook, N.J., Mumm, A.S., Giles, D., 2013. Uranium-bearing hematite from the Olympic Dam Cu-U-Au deposit, South Australia: A geochemical tracer and reconnaissance Pb-Pb geochronometer. Precambrian Research, 238: 129-147.

Cockerton, A.B., and Tomkins, A.G. (2012) Insights into the Liquid Bismuth Collector Model Through Analysis of the Bi-Au Stormont Skarn Prospect, Northwest Tasmania. Economic Geology, 107, 667-682.

Conradson, S.D. (1998) Application of X-ray absorption fine structure spectroscopy to materials and environmental science. Applied Spectroscopy, 52, 252A.

Cook, N.J., Ciobanu, C.L., Brugger, J., Etschmann, B., Howard, D.L., De Jonge, M.D., Ryan, C. and Paterson, D. (2012) Determination of the oxidation state of Cu in substituted Cu-In-Fe-bearing sphalerite via μ-XANES spectroscopy. American Mineralogist, 97, 476-479.

Cuney, M. (2009) The extreme diversity of uranium deposits. Mineralium Deposita, 44, 3-9.

Fritsche, R., and Dahlkamp, F. (1997) Contribution to characteristics of uranium oxides. Assessment of uranium deposit types and resources-a worldwide perspective. Proc Tech Comm Meeting, IAEA and OECD Nuclear Energy Agency, Vienna.

Grønvold, F. (1955) High-temperature X-ray study of uranium oxides in the UO_2-U_3O_8 region. Journal of Inorganic and Nuclear Chemistry, 1, 357-370.

Hitzman, M.W., Oreskes, N., and Einaudi, M.T. (1992) Geological characteristics and tectonic setting of proterozoic iron oxide (Cu-U-Au-REE) deposits. Precambrian Research, 58, 241-287.

Hitzman, M.W., and Valenta, R.K. (2005) Uranium in iron oxide-copper-gold (IOCG) systems. Economic Geology, 100, 1657-1661.

Keller, R., Wrcoff, H., and Marchi, L.E. (1946) Copper (I) chloride. Inorganic Syntheses, Volume 2, 1-4.

Nevin, K.P., and Lovley, D.R. (2000) Potential for nonenzymatic reduction of Fe (III) via electron shuttling in subsurface sediments. Environmental science & technology, 34, 2472-2478.

453 Okrugin, V.M., Andreeva, E., Etschmann, B., Pring, A., Li, K., zhao, J., Griffins, G.,
454 Lumpkin, G.R., Triani, G., and Brugger, J. (2014) Microporous Au:
455 comparison of textures from Nature and experiments. American
456 Mineralogist, 99, 1171–1174.
457 Ord, A., Hobbs, B.E., Lester, D.R., 2012. The mechanics of hydrothermal systems: I.
458 Ore systems as chemical reactors. Ore Geology Reviews, 49: 1-44.
459 Putnis, A. (2009) Mineral replacement reactions. Reviews in mineralogy and
460 geochemistry, 70, 87-124.
461 Putnis, A., and John, T. (2010) Replacement processes in the Earth's crust. Elements,
462 6, 159-164.
463 Qian, G., Brugger, J., Skinner, W.M., Chen, G., and Pring, A. (2010) An
464 experimental study of the mechanism of the replacement of magnetite by
465 pyrite up to 300 ˚C. Geochimica et Cosmochimica Acta, 74, 5610-5630.
466 Rickard D. and Luther, III, G. W. (2007) Chemistry of iron sulfides. Chemical
467 Review, 107, 514–562.
468 Shavarov, Y.V., Bastrakov, E. (1999) HCh: a software package for geochemical
469 equilibrium modelling (user's guide). 61 pp.
470 Singh, Y., Viswanathan, R., Parihar, P.S., and Maithani, P.B. (2011) X-Ray
471 crystallography of uraninite from proterozoic sedimentary basins of
472 peninsular India: Implications for uranium ore genesis. The Indian
473 Mineralogist, 45, 1-30.
474 Slack, J.F., M.P., F., and Flohr, M.J.K. (2003) Exhalative and subsea-floor
475 replacement processes in the formation of the Bald Mountain massive sulfide
476 deposit, Northern Maine. Economic Geology Monography, 11, 513-547.

Tenailleau, C., Pring, A., Etschmann, B., Brugger, J., Grguric, B., and Putnis, A. (2006) Transformation of pentlandite to violarite under mild hydrothermal conditions. American Mineralogist, 91, 706-709.

Tooth, B.A., Brugger, J., Ciobanu, C. and Liu, W. (2008) Modeling of gold scavenging by bismuth melts coexisting with hydrothermal fluids. Geology, 36, 815-818.

Tooth, B., Ciobanu, C.L., Green, L., O'Neill, B., and Brugger, J. (2011) Bi-melt formation and gold scavenging from hydrothermal fluids: An experimental study. Geochimica et Cosmochimica Acta, 75, 5423-5443.

Wülser, P.-A., Meisser, N., Brugger, J., Schenk, K., Ansermet, S., Bonin, M., and Bussy, F. (2005) Cleusonite, $(Pb,Sr)(U^{4+},U^{6+})(Fe^{2+},Zn)_2(Ti,Fe^{2+},Fe^{3+})_{18}(O,OH)_{38}$, a new mineral species of the crichtonite group from the western Swiss Alps. European journal of mineralogy, 17, 933-942.

Yamamoto, Y., Takahashi, Y., Kanai, Y., Watanabe, Y., Uruga, T., Tanida, H., Terada, Y., and Shimizu, H. (2008) High-sensitive measurement of uranium L_{III}-edge X-ray absorption near-edge structure (XANES) for the determination of the oxidation states of uranium in crustal materials. Applied Geochemistry, 23, 2452-2461.

Zhao, J., Brugger, J., Grundler, P.V., Xia, F., Chen, G., and Pring, A. (2009) Mechanism and kinetics of a mineral transformation under hydrothermal conditions: Calaverite to metallic gold. American Mineralogist, 94, 1541-1555.

Zhao, J., Brugger, J., Nogthai, Y., and Pring, A. (2014) The formation of chalcopyrite and bornite under hydrothermal conditions: an experimental approach. American Mineralogist, 99, 2389-2397..

Zhao, J., Brugger, J., Xia, F., Ngothai, Y., Chen, G., and Pring, A. (2013) Dissolution-reprecipitation vs. solid-state diffusion: Mechanism of mineral transformations in sylvanite, $(AuAg)_2Te_4$, under hydrothermal conditions. American Mineralogist, 98, 19-32.

509 # Figure captions

510

511 **Figure 1**. SEM images of reaction products for Cu-bearing experiments. All
512 reactions were conducted in $pH_{25^\circ C}$ 5 acetate buffer and 1 m NaCl solutions, in the
513 presence of CuCl and thioacetamide. Uraninite ($UO_{2+x(S)}$) was added as a U-source in
514 **(b-d)**. **(a)** Hematite particle with chalcopyrite rim in U-free run (2 weeks, 300 ^{o}C). **(b)**
515 Typical grains obtained in runs with $UO_{2+x(S)}$ as U-source (2 weeks, 300 ^{o}C). Note
516 inclusions of uraninite grains in the overgrowth chalcopyrite in **(b)**. **(c)** FIB cut of
517 grain (red line in **(b)**). **(d)** EDAX chemical map of area in **(c)**.

518

519 **Figure 2**. SEM images of reaction products for Cu-free experiments. All reactions
520 were conducted in a $pH_{25^\circ C}$ 5 acetate buffer and 1 m NaCl at 300 ^{o}C for 1 week,
521 showing the effect of the addition of uraninite **(a,b)** and uraninite+thioacetamide
522 **(c,d)**. No reaction was observed in the buffer-only runs. Note the pyrite rim and
523 uranium-rich line in **(c,d)**. The dotted line in (d) emphasizes the pyrite-oxide
524 boundary.

525

526 **Figure 3**. Reaction products and textures for Cu-bearing experiments with
527 $UO_2(NO_3)_2$ as a U-source. All reactions were conducted in $pH_{25^\circ C}$ 5 acetate buffer
528 and 1 m NaCl solutions, in the presence of CuCl and thioacetamide. **(a,b)** 2 hours,
529 300 ^{o}C; (**c,d,e**) 2 weeks, 300 ^{o}C. **(a-d)** SEM images; (**e**) EDAX chemical map of the
530 grain shown in **(c)**.

Figure 4. XANES spectra **(a)** and their first derivative **(b)** for U-mineral standards for U in the U-rich lines of sample from 2 weeks reaction at 300 ^{o}C in $pH_{25^{\circ}C}$ 5 acetate buffer and 1 m NaCl solutions using uraninite ($UO_{2+x(S)}$) as a U-source.

Figure 5. SEM image of uranium (uraninite/coffinite) associated with hematite and chalcopyrite from Olympic Dam, South Australia. Fluorite is the matrix mineral.

a

Hem

Cpy

U-Free
2Weeks 220 ºC

100µm

b

Uraninite

With UO_{2+x}
2Weeks 300ºC

50µm

C

Hem ± Mag ± Py

Cpy

U

Py

2µm

d

S

Cu

U

2µm

a

Buffer-UO_2
1Week 300 ºC

50µm

b

40µm

c

Buffer-UO_2-Thioacetamide
1Week 300 ºC

50µm

d

10µm

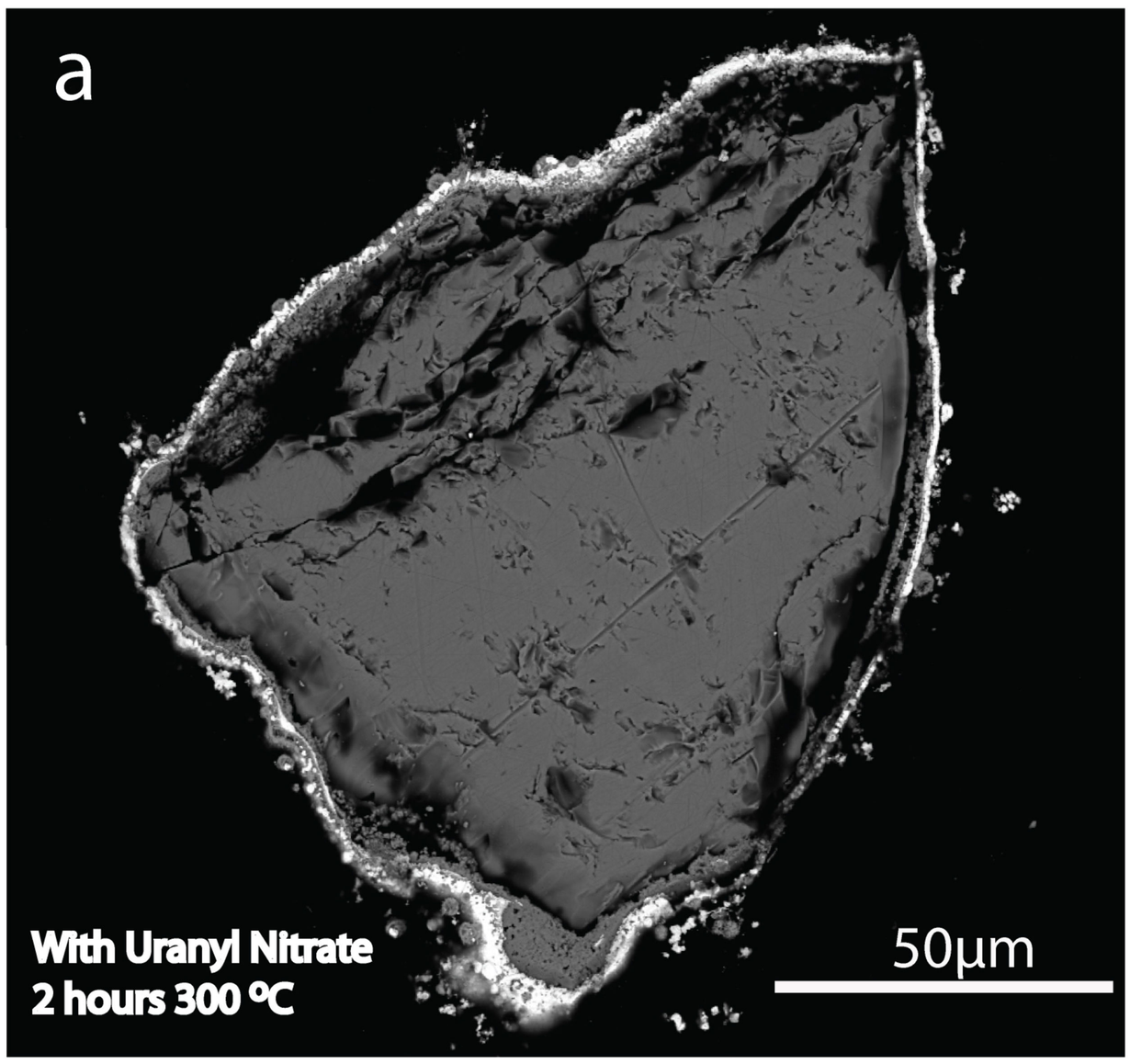
a
With Uranyl Nitrate
2 hours 300 ºC
50µm

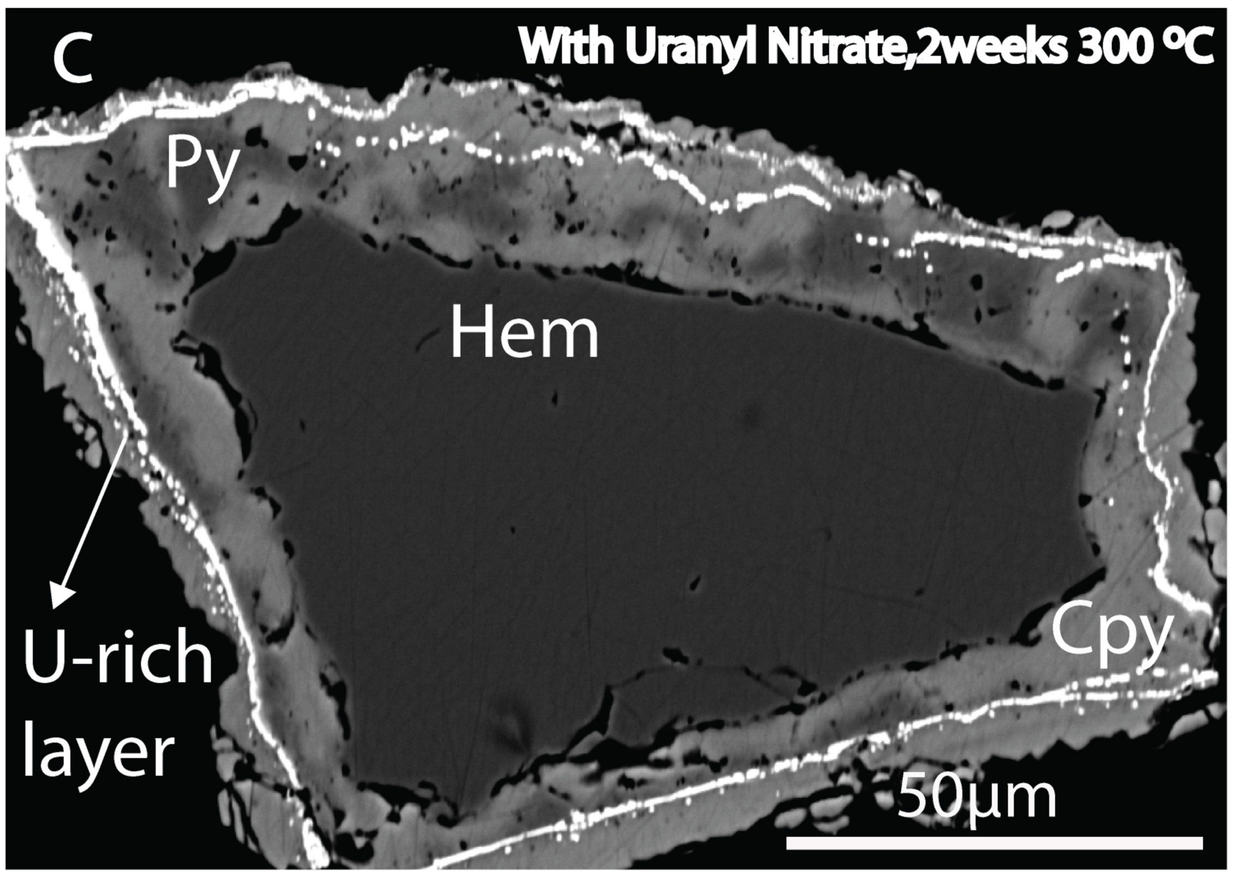
C
With Uranyl Nitrate,2weeks 300 ºC
Py
Hem
Cpy
U-rich
layer
50µm

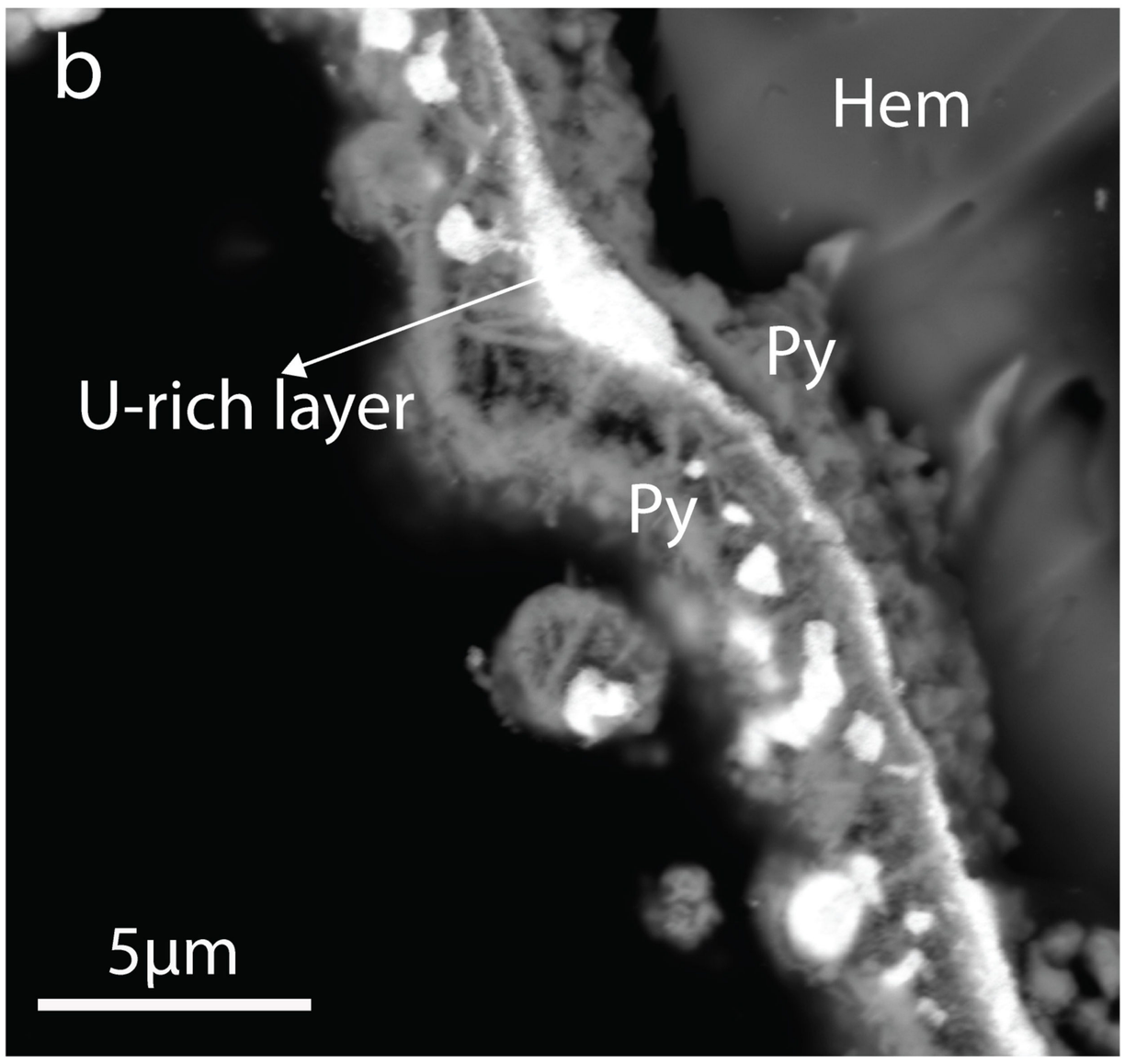
b
Hem
Py
U-rich layer
Py
5µm

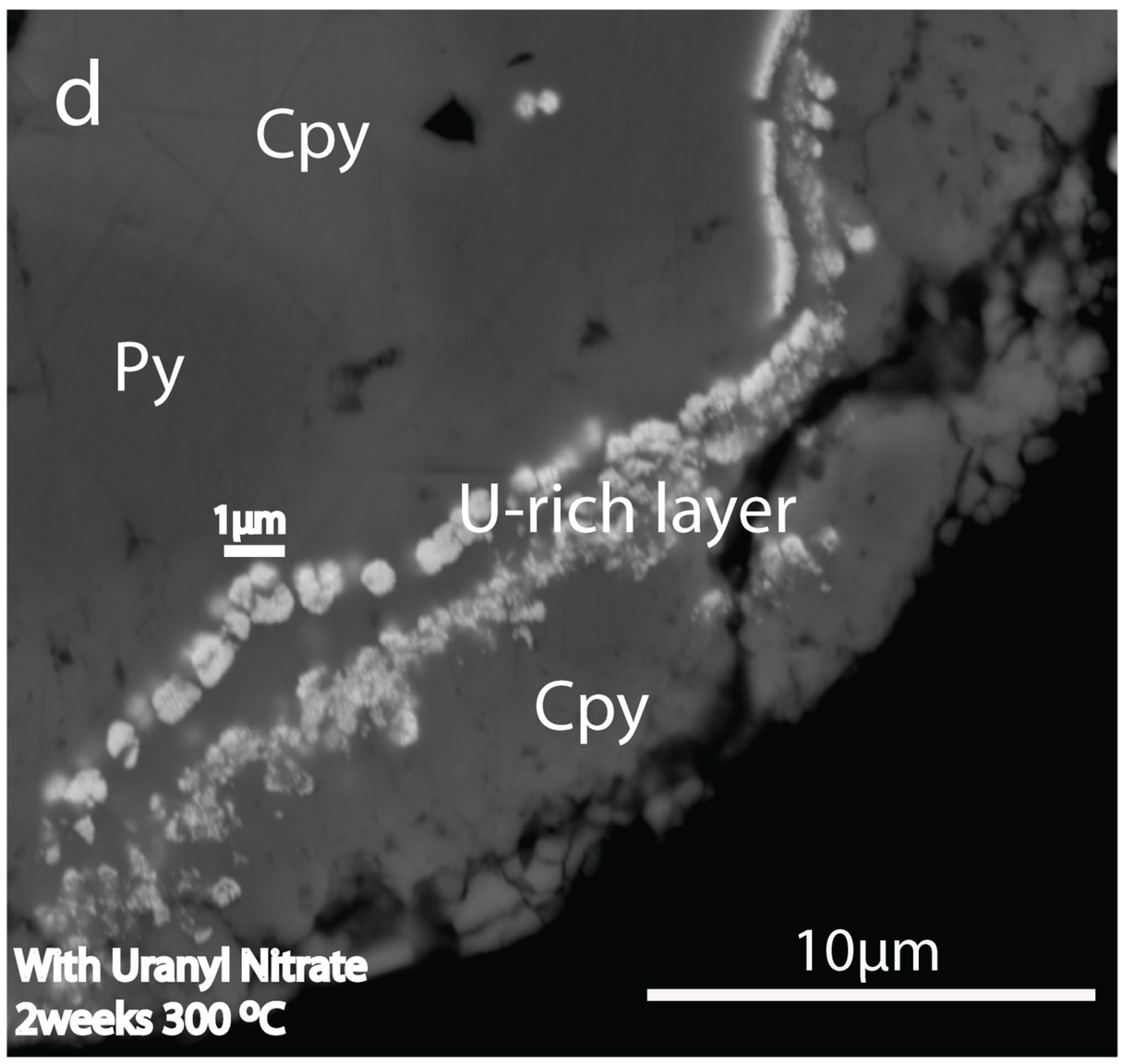
d
Cpy
Py
1µm
U-rich layer
Cpy
With Uranyl Nitrate
2weeks 300 ºC
10µm

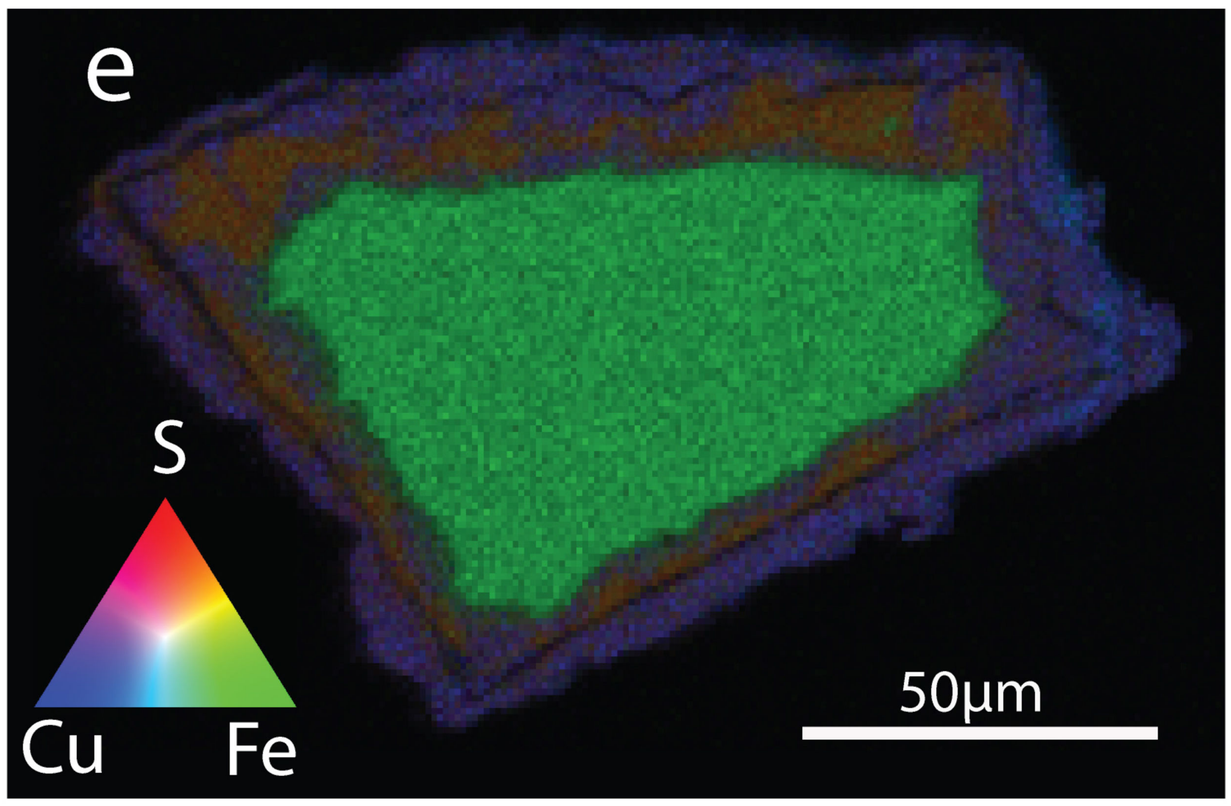
e
S
Cu
Fe
50µm

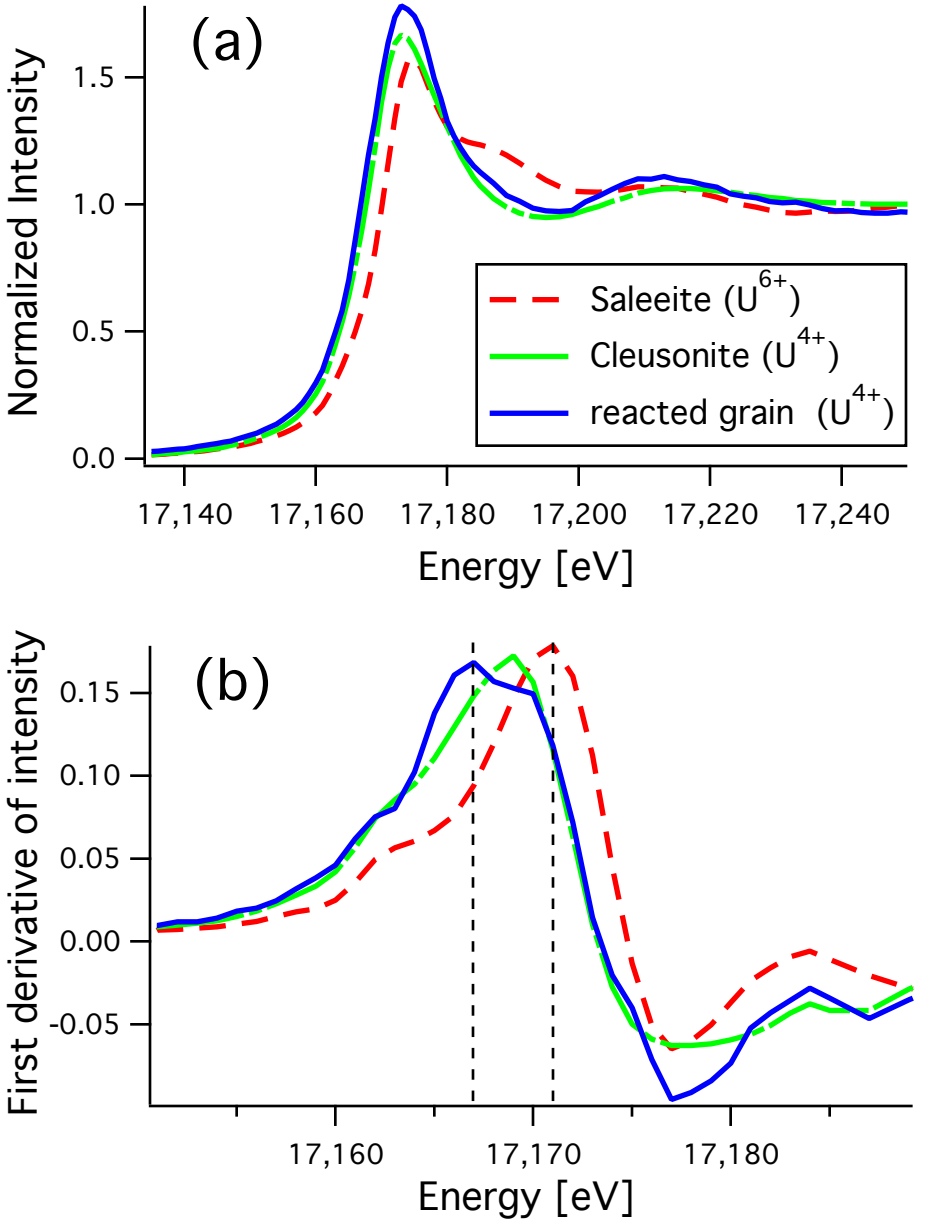
(a)
Normalized Intensity
1.5
1.0
0.5
0.0
Saleeite (U^{6+})
Cleusonite (U^{4+})
reacted grain (U^{4+})
17,140
17,160
17,180
17,200
17,220
17,240
Energy [eV]
(b)
First derivative of intensity
0.15
0.10
0.05
0.00
-0.05
17,160
17,170
17,180
Energy [eV]

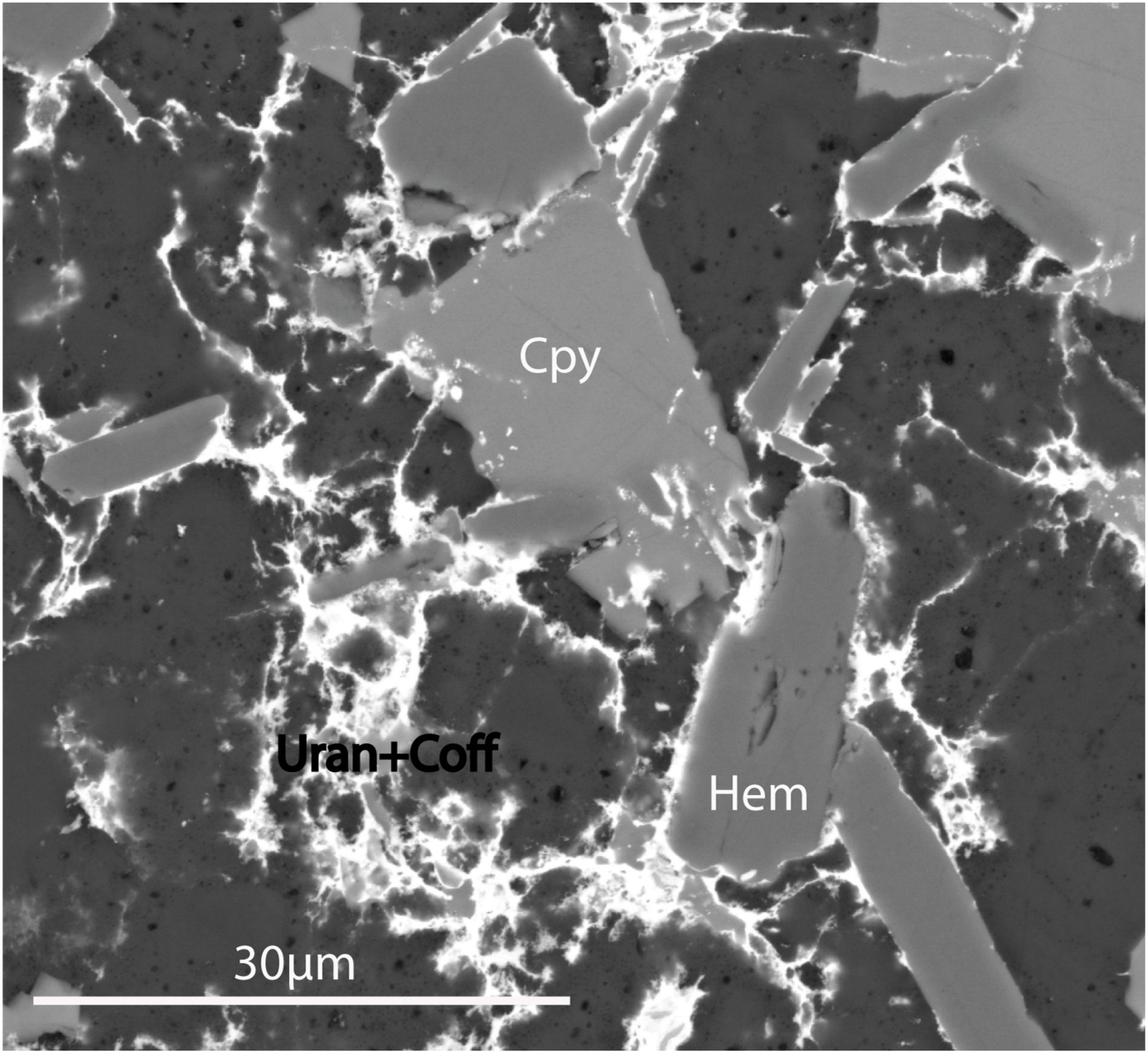
Cpy
Uran+Coff
Hem
30µm